Elementary mechanisms of shear-coupled grain boundary migration for different complexions of a copper tilt grain boundary

Swetha Pemma,[1] Rebecca Janisch,[2] Gerhard Dehm,[1,*] and Tobias Brink[1,†]

[1] *Max-Planck-Institut für Eisenforschung GmbH, Max-Planck-Straße 1, 40237 Düsseldorf, Germany*
[2] *Interdisciplinary Centre of Advanced Materials Simulation (ICAMS), Ruhr-Universität Bochum, 44780 Bochum, Germany*

(Dated: May 18, 2023)

The migration of grain boundaries leads to grain growth in polycrystals and is one mechanism of grain-boundary-mediated plasticity, especially in metallic nanocrystals. This migration is due to the movement of dislocation-like defects, called disconnections, which couple to externally applied shear stresses. Here, we investigate a Σ19b symmetric tilt grain boundary without pre-existing defects using atomistic computer simulations with classical potentials. This specific grain boundary exhibits two different atomic structures with different microscopic degrees of freedom (complexions), called "domino" and "pearl" complexion. We show that the grain boundary migration is affected by both the formation energy of a disconnection dipole and the Peierls-like barrier required to move the disconnections. For the pearl complexion, the latter is much higher, leading to a high stress required for grain boundary migration at low temperatures. However, in absolute values, the Peierls barrier is low and can be overcome by thermal energy even at room temperature. Since the domino complexion has higher disconnection formation energies, it is more resistant to migration at room temperature and above.

I. INTRODUCTION

Grain boundaries (GBs) influence mechanical properties of polycrystalline materials and GB engineering is critical in material design [1]. The motion of GBs is the key factor in the microstructure evolution of poycrystalline materials [2, 3]. When subjected to shear stress, GBs move and can account for part of the plastic deformation in nanocrystalline materials [4–7]. Some of the GB deformation mechanisms discussed in the literature are GB sliding [8–10], grain rotation [11–15], shear coupled GB migration [16–32], diffusional creep [6, 33], dislocation interaction at grain boundaries [4, 6, 33, 34], and enhanced partial dislocation activity [4, 6, 33, 34].

Shear coupling is the migration of GBs driven by shear stress across the GB plane [19, 24, 35]. It can lead to complex effects during grain growth in a polycrystal such as grain rotation, stress generation, and grain growth stagnation, which are all inter-related [15]. A shear coupling factor $\beta = v_\parallel / v_\perp$ describes how a GB migrates: A relative shear velocity $v_\parallel$ of the two grains parallel to the GB is coupled directly to the GB migration velocity $v_\perp$ normal to its plane [12, 19, 36, 37]. This factor β is influenced by parameters such as temperature, bicrystallography, and the type of the driving force [38]. Microscopically, shear-coupled motion is caused by the movement of disconnections, which are line defects at the GB [36, 37, 39, 40]. Disconnections have dislocation character insofar that they have a Burgers vector **b**, which couples to externally applied stress. They also lead to a step of size h in the GB, which results in the GB migration during disconnection nucleation and movement [35, 41]. The formation and migration of disconnections play a vital role in the kinetic properties of GBs [42–46] and pre-existing mobile disconnections lead to a reduced stress required for GB migration [47]. Bicrystallography influences the possible disconnection modes, i.e., which Burgers vectors can occur, and the applied stress and temperature influence the active disconnection mode [19, 37, 38, 45, 48, 49].

At the atomic scale, however, different structures at GBs and first-order transitions between them were observed even in pure metallic materials [50–57]. These different structures can be treated as interface phases, which can only exist in contact with the abutting crystallites, and can be treated using a thermodynamic framework [58–63]. They are called complexions [64–67] or GB phases [68]. Complexion transitions, then, are analogous to bulk phase transitions: The GB structure, composition, and properties change discontinuously at critical values of thermodynamic parameters such as temperature, pressure, and chemical potential [62–64, 66–68]. Only a few simulation studies investigated the influence of complexion transitions on the shear coupled motion. They found that β can depend on the complexion present at the GB, even if the macroscopic degrees of freedom of the GB are constant (congruent complexion transition [66]) and only the microscopic degrees of freedom change [19, 69]. The understanding of how complexion transitions can affect shear-coupled GB migration from a mechanistic viewpoint is thus still at its infancy.

In this paper, we report the underlying mechanisms and parameters of shear-coupled motion for a Σ19b $[11\bar{1}]$ (178) symmetric tilt GB. This GB can exhibit two different complexions [55]. We discuss the disconnection mode that is active in these complexions and how differences of disconnection formation and migration energies affect the GB migration.

* dehm@mpie.de
† t.brink@mpie.de

II. COMPUTATIONAL METHODS

We studied bicrystals with symmetric tilt GBs using molecular dynamics (MD) simulations, which were performed using LAMMPS [70, 71] with the embedded atom method (EAM) potential of Mishin et al [72]. This potential reproduces some properties of Cu very well, comprising elastic constants, phonon frequencies, thermal expansion, intrinsic stacking fault energy, the coherent twin boundary energy and others. We used a time integration step of 2 fs for all dynamics simulations.

The bicrystals for Σ19b $[11\bar{1}]$ (178) symmetric tilt GBs (misorientation of 46.83°) were created by constructing two fcc crystals with the desired crystallographic orientations $[\bar{5}3\bar{2}]$, [178], $[11\bar{1}]$ in x, y, z directions for the top crystal and $[\bar{3}52]$, [718], $[11\bar{1}]$ for the bottom crystal [Fig. 1(a)]. Here, y is the GB normal and z the tilt axis. The x and z directions were periodic and we used open boundaries in y direction, allowing us to produce differently-sized cells by repeating the unit cell along the periodic directions. The periodic unit cell dimensions were $L_x = 11.142$ Å and $L_z = 6.261$ Å. We used L_y ranging from 385.317 Å to 5790.070 Å (see below). The GB structures were formed by combining the two crystallites, sampling the microscopic degrees of freedom by displacing the top crystal, and minimizing the result in molecular statics (γ-surface method). We did this until the previously reported pearl and domino complexions [55] were found (we evaluated that structure, GB energy, and excess volume match). The minimum energy GB structures for domino and pearl are visualized using OVITO [73] and are shown in Fig. 2(a)–(b).

For the simulation of shear-coupled GB motion, we used a simulation cell of size $222.814 \times 385.317 \times 62.613$ Å^3 ($20 \times 20 \times 10$ unit cells, resulting in 455,400 atoms) unless specified otherwise.

We started by using molecular statics simulations ($T = 0$ K) and applying a displacement on the top boundary in x direction and keeping the bottom boundary fixed. Both boundaries were the regions at the surfaces in y direction each with a width of 55 Å [Fig. 2(c)–(d)]. To study GB migration in domino and pearl, the shear displacement d was applied stepwise in increments of 0.05 Å, while minimizing the system after every step. We calculated the resulting shear stress by dividing the reaction force at the boundary by the area $L_x \times L_z$ of the top boundary.

Then, MD simulations were performed in the canonical ensemble (Nosé–Hoover thermostat at $T = 100$, 200, 300, 400, 500, 600 K). At finite temperatures, the system was scaled to obtain the correct lattice constant at the desired temperature T and then equilibrated for 4 ns. In this simulation procedure, we applied a velocity in x direction to the top boundary, while keeping the bottom boundary fixed (see Ref. [19] and Fig. 2). The top boundary was allowed to move freely in y and z direction. Shear-coupled simulations were performed for shear velocities in the range from 0.01 m/s to 10 m/s. We typically applied a constant shear velocity of 0.1 m/s unless otherwise noted. Shear stress was calculated as for the molecular statics simulations.

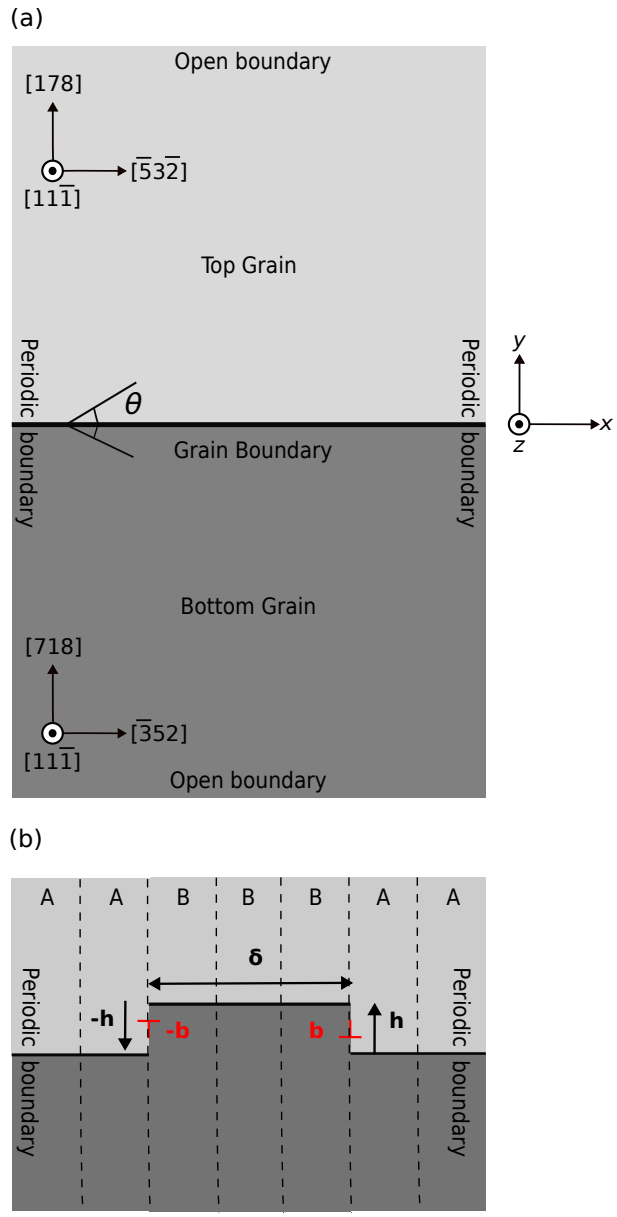

FIG. 1. (a) Schematic of the bicrystallography of a Σ19b $[11\bar{1}]$ (178) symmetric tilt GB. Top and bottom fcc crystals are joined in the indicated orientations, leading to a misorientation between the two crystals of 46.83°. (b) Schematic of the construction of the disconnection dipole with opposite Burgers vetor by repeating bicrystals A and B. Bicrystal B is moved by a translation vector and step height compared to A. By varying the number of B unit cells, the separation δ between disconnections can be controlled.

The desired disconnection dipoles were constructed for different disconnection widths δ (separation distance between the two disconnections). This is similar to the con-

struction of disconnection as described in Refs. [74, 75]: Bicrystals A and B were generated such that they contain the same complexion. The GB in bicrystal B was moved by one step height compared to A. By replicating A and B and assembling them (e.g., as AABBBAA), two disconnections with opposite Burgers vector appear at the junctions ...AB... and ...BA... [Fig. 1(b)]. By varying the number of B unit cells, the separation δ between disconnections can be controlled. We calculated the energy of the disconnection dipoles in simulation cells of sizes ranging from $1114.220 \times 964.490 \times 6.261\,\text{Å}^3$ (5.6×10^5 atoms) to $1114.220 \times 5790.070 \times 6.261\,\text{Å}^3$ (3.4×10^6 atoms) to ensure that size effects due to the open boundary condition in y could be excluded and that the results converged.

Monopoles (single disconnections) were constructed in a similar way by combining A and B so that only one disconnection occurs (...AAABBB...) and by leaving open boundaries in x direction. Simulation cell sizes ranging from $2228.830 \times 1949 \times 6.261\,\text{Å}^3$ (2.3×10^6 atoms) to $3342.799 \times 5790.07 \times 6.261\,\text{Å}^3$ (1.0×10^7 atoms) with open boundary conditions in x and y directions were investigated. We computed the monopole energy in a region of size $L_x/2 \times L_y/2 \times L_z$ in the center of the simulation cell. We varied L_x and L_y to observe convergence of the monopole energies, but could not achieve any convergence with L_x due to the infinitely long-ranged elastic interaction between the Burgers vector and the surfaces.

Finally, in order to obtain the barriers for the migration of the disconnections themselves, the minimum energy path for a change of the disconnection dipole width δ was obtained by nudged elastic band (NEB) method calculations [76, 77]. The spring constants for the parallel and perpendicular nudging forces were both $1.0\,\text{eV}/\text{Å}^2$. The minimization scheme used was quickmin [78]. The initial and final states of the minimum energy path are the GB structures with disconnection dipole widths δ varying by 11.142 Å (equivalent to a CSL periodicity vector and thus the distance between two local minima for the disconnections). The saddle point observed along the minimum energy path is the required disconnection migration barrier (difference in minimum and maximum energy observed along minimum energy path).

Raw data for all simulations and analyses is available in the companion dataset [79].

III. RESULTS AND DISCUSSION

A. Shear coupling

In the present work, we investigated $\Sigma 19$b $[11\bar{1}]$ (178) symmetric tilt GBs in copper. For these GBs, two different complexions can occur [55], named domino [Fig. 2(a)] and pearl [Fig. 2(b)]. These complexions each consist of two structural units, here designated as ...RLRLRL....

We simulated the shear-coupled motion of these two complexions by applying a shear displacement. The result for the applied shear velocity of 0.1 m/s after a simulation time of 20 ns at 300 K is shown in Fig. 2(c)–(d). Before the simulations, atoms in a vertical line were marked in yellow. This fiducial line highlights the atomic displacements: The GB has moved in positive y direction from its original position (dashed line), while the material was sheared in positive x direction. The macroscopically applied displacement couples thus to the GB migration. The slope of the fiducial line provides the ratio of GB migration distance to sliding and is therefore equivalent to the inverse of the shear coupling factor [12, 19, 36, 37]

$$\beta = \frac{v_\parallel}{v_\perp}, \tag{1}$$

where $v_\parallel$ is the shear velocity applied to the system and $v_\perp$ the velocity of GB migration. To more accurately calculate β, we can record the displacement u_x of the atoms and plot it as a function of the atomic position normal to the GB (Fig. 3). The slope can be obtained by linear regression and corresponds directly to β. Earlier studies show that β is a characteristic of a GB and depends on the misorientation of top and bottom crystal [19], but can also depend on the complexion for fixed macroscopic GB parameters [69]. In this study, β is observed to be 0.874 for both domino and pearl. This is independent of the applied shear velocity or temperature, see Fig. S1 in the Supplemental Material (SM) [80]. We note, however, that the individual displacements u_x of atoms at a certain y position in the region traversed by the GB depend on the complexion. We observe three distinct offsets of the displacement u_x of atoms in domino (with the same slope), but only one in pearl. This hints at differences of the internal atomic shuffling during GB migration in domino and pearl.

In these simulations, displacement was imposed and the GB migration velocity $v_\perp$ only depends on the applied shear velocity $v_\parallel$ and β. In reality, it is often the case that a given stress is applied, so a relevant figure of merit is the critical stress τ_c required to start GB migration. This can be obtained by monitoring the reaction forces at the boundary where the shear is applied. We started with deformation in molecular statics ($T = 0\,\text{K}$). As the displacement d increases, the shear stress τ increases linearly in the elastic regime (Fig. 4). At a certain displacement, the shear stress drops as the GB migrates. The critical shear stress τ_c is observed to be 1.117 GPa for pearl and 0.849 GPa for domino. As we increase the displacement, the GB continues to move, resulting in recurring shear stress drops at intervals of displacement characteristic to the simulation cell size. This saw-tooth behavior is similar to earlier reported simulation studies [19, 21, 22, 27]. The pearl complexion has a significantly higher barrier for GB migration than the domino complexion.

By unloading the system after the first stress drop down to zero shear stress, we obtain a residual displacement of $d_s \approx 0.550$ Å (marked in the inset of Fig. 4). The distance h traveled by the GB during the event is obtained from atomistic simulations by marking the equiv-

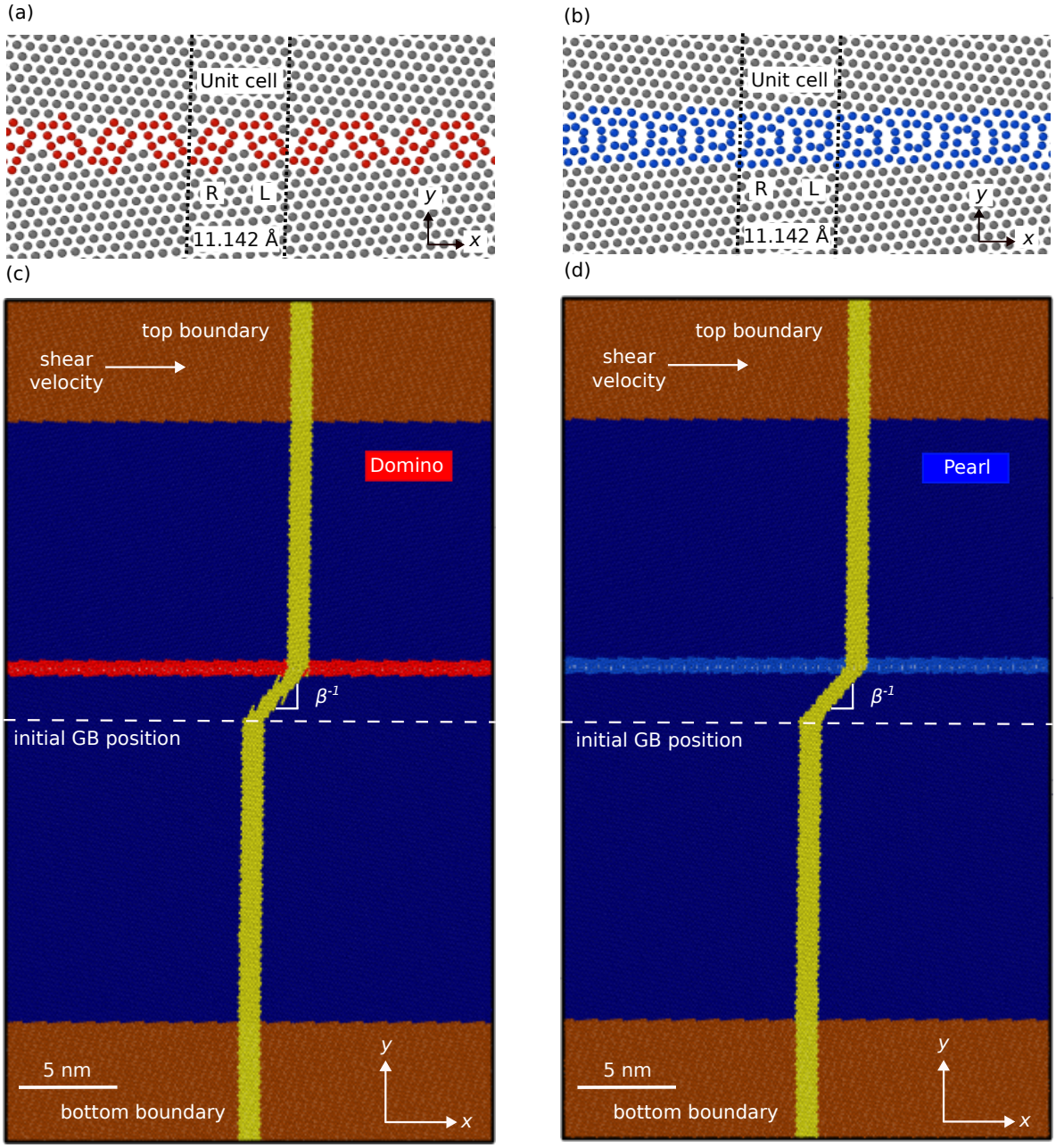

FIG. 2. Atomic structures of the (a) domino and (b) pearl complexions in our computer model. Both complexions consist of two repeating structural units (...RLRLRL...). Shear coupling simulations for 20 ns with a shear velocity of 0.1 m/s at 300 K lead to a migration distance on the order of 2 nm for both (c) domino and (d) pearl. Shear coupled GB motion is highlighted by the yellow fiducial mark, which exhibits a slope (equivalent to β^{-1}) in the region traversed by the GB. The top grain is sheared and the bottom grain grows at the expense of the top grain.

alent position in the structural unit (e.g., in R) along y in the initial and final GB positions. Together with the distance $h \approx 0.647$ Å that the GB traveled during the event, we again obtain $\beta = d_s/h \approx 0.850$ for domino and $h \approx 0.686$ Å, $\beta = d_s/h \approx 0.801$ for pearl. The difference in β is due to the relatively large error of determining h from a single GB migration step, and the values from Fig. 3 should be preferred. We also observe that the structural units in both complexions switch from ...RLRLRL... to ...LRLRLR..., which indicates that the migration is related to the atomic structure, but that the basic character of the GB is preserved during migra-

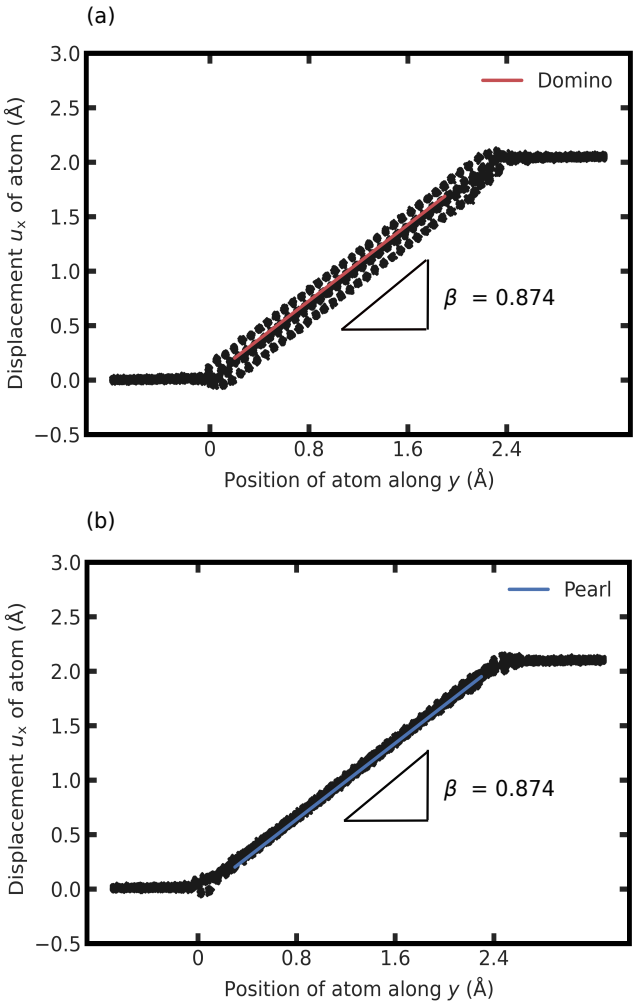

FIG. 3. Displacement u_x of atoms as a function of their position along the y axis for the (a) domino and (b) pearl complexions during the shear-coupling simulations. Note that $y = 0$ corresponds to the initial GB position. The shear coupling factor β is the slope (red and blue lines) of these graphs and was obtained by linear regression (Eq. 1). The regions belonging to the bottom crystal ($y < 0$ Å, zero displacement) and to the top crystal ($y > 2.4$ Å) are strain-free (constant displacement), while the region traversed by the GB was sheared.

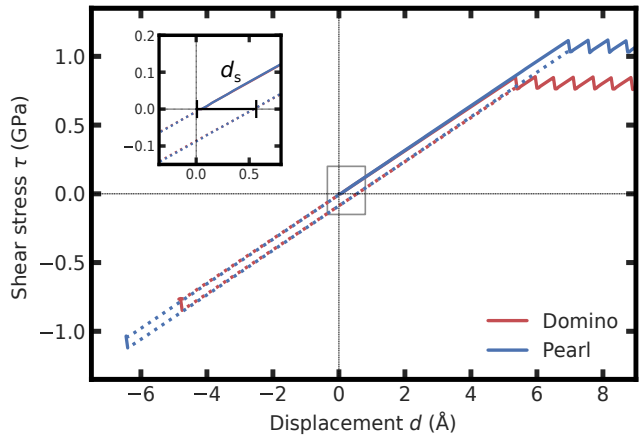

FIG. 4. Shear stress response to displacement at 0 K plotted for domino and pearl. Each shear stress drop observed corresponds to a unit step GB migration. The maximum shear stress is the critical shear stress τ_c required for GB migration. The dotted lines represent unloading followed by loading in the opposite direction after the first stress drop. The inset shows the shear deformation d_s for GB migration by a unit step. The shear deformation is observed to be ≈ 0.550 Å for both domino and pearl. The migration normal to the GB plane from the initial position obtained from atomistic simulations is ≈ 0.647 Å and ≈ 0.686 Å for domino and pearl respectively.

tion. We will now investigate the atomistic mechanism behind the difference in critical stresses.

B. Atomistic mechanisms and bicrystallography

It is known that line defects with dislocation character can exist on GBs [35–37, 39–41]. These are called secondary GB dislocations or disconnections and possess both a Burgers vector **b** (leading to the dislocation character) and a step height h. Disconnections can only exist on and move along the GB, where they also introduce a step of the GB plane. The Burgers vector is associated with a long-range strain field. Applied shear couples to this strain field, and the GB migrates due to the step of the disconnections, which nucleate and propagate under the stress. Similar to a bulk dislocation, the structure of the GB on both sides of the disconnection is undisturbed. Thus, the Burgers vectors must be displacement shift complete (DSC) vectors. We found that the disconnection that is active during GB migration in both domino and pearl is $(\mathbf{b}, h) = ([0.586, 0, 0]\,\text{Å}, 0.677\,\text{Å})$, resulting in $\beta = b_x/h = 0.865$ (see Appendix A).

During a unit GB migration step, we found that the atoms do not jump immediately from their initial to their final positions in the respective fcc lattices of the top and bottom crystal, indicating that the GB has a certain width in which the equilibrium positions do not correspond to crystallographic sites in fcc (see Appendix B for more details). The differences in atomic shuffling between domino and pearl, however, did not provide a conclusive reason for the difference in critical stress τ_c for GB migration.

C. Disconnection monopoles and dipoles

When disconnections nucleate in otherwise defect-free GBs, a pair of opposite disconnections, namely $(\mathbf{b}, h)$ and $(-\mathbf{b}, -h)$, has to be created. This would be similar for bulk dislocations. These disconnections form a disconnection dipole with a separation δ between disconnections.

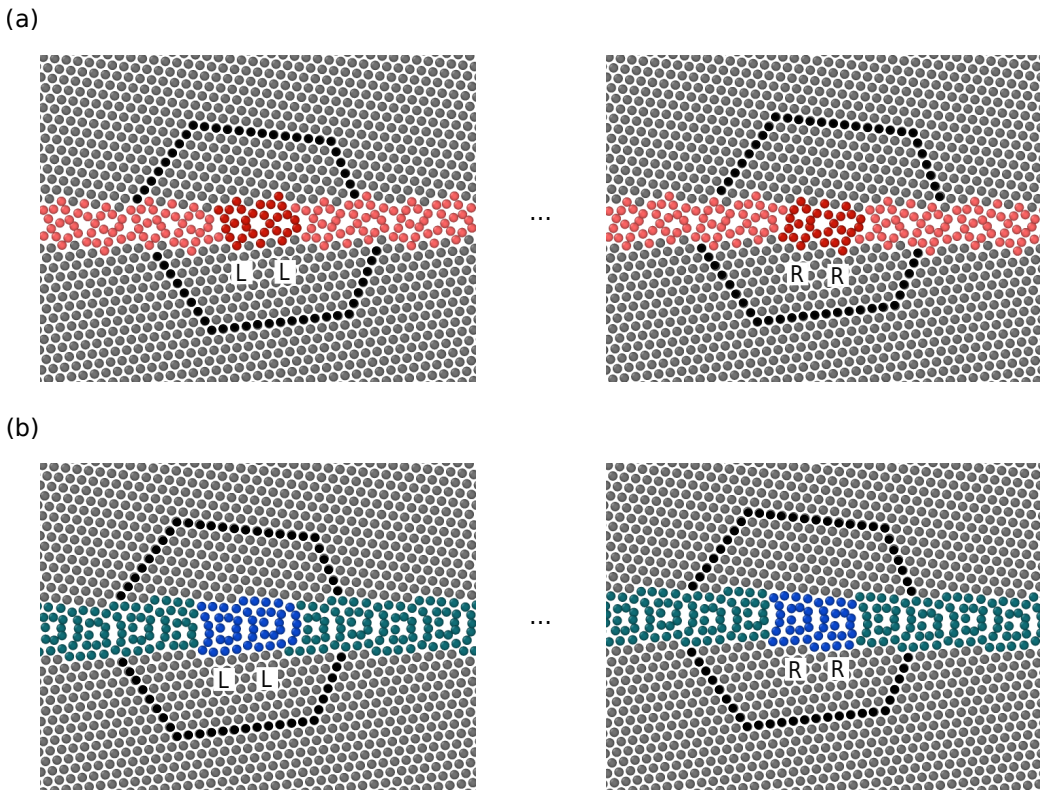

FIG. 5. Structure of the disconnection dipoles in (a) domino and (b) pearl. On the left, the disconnection is ($\mathbf{b} = [0.586, 0, 0]$ Å, $h = 0.677$) with structural units ...LRLR**LL**RLRL.... On the right, we have the opposite disconnection ($\mathbf{b} = [-0.586, 0, 0]$ Å, $h = -0.677$) with structural units ...RLRL**RR**LRLR... The disconnection dipoles were constructed for different disconnection dipole widths δ. In the image, the ellipsis indicates that δ is larger than visible. Burgers circuits are drawn around the disconnections (black atoms) to verify the disconnection mode obtained after minimization.

TABLE I. GB energies and parameters K and δ_0 for the dipole energies obtained from fitting Eq. (6) to E_{dipole} from the simulations. We list the GB energy γ^* including a disconnection dipole with $\delta = L_x/2$, the parameter K describing anisotropic crystal elasticity, and the effective disconnection core size δ_0. The energy differences are always $\Delta E = E_{\text{domino}} - E_{\text{pearl}}$, with $\Delta E^*_{\text{dipole}}$ being the dipole energy difference at $\delta = L_x/2$, and $\Delta E_{\text{monopole}}$ being the energy difference between monopoles (single disconnection). With the latter, we can also extract the difference of the elastic interaction energies $\Delta E_{\text{elastic}}$ and the ratio of disconnection core sizes $\delta_c^{\text{domino}}/\delta_c^{\text{pearl}}$.

L_y (Å)	964.490	1929.540	3859.800	5790.070
γ^*_{domino} (J/m^2)	0.872	0.873	0.873	0.873
K_{domino} (meV/Å^3)	41.9	75.6	77	76.8
δ_0^{domino} (Å)	0.191	3.540	3.791	3.761
γ^*_{pearl} (J/m^2)	0.836	0.837	0.837	0.837
K_{pearl} (meV/Å^3)	40.6	75	76.4	76.4
δ_0^{pearl} (Å)	0.211	4.067	4.358	4.366
$\Delta E^*_{\text{dipole}}$ (meV/Å)	4.885	4.567	4.557	4.555
$2\Delta E_{\text{monopole}}$ (meV/Å)	–	5.718	5.549	5.661
$\Delta E_{\text{elastic}}$ (meV/Å)	–	−1.151	−0.992	−1.105
$\delta_c^{\text{domino}}/\delta_c^{\text{pearl}}$	–	1.045	1.038	1.042

Due to the opposite signs of the Burgers vectors, the disconnections in the dipole have an attractive interaction. We created dipoles of different widths in domino and pearl GBs to evaluate their energy. The smallest possible stable dipole width is 11.142 Å, corresponding to the GB unit cell size along ⟨532⟩. To introduce the dipole, part of the GB is translated and moved with the desired $\mathbf{b}$ and h and the energy of the entire structure is minimized. Parts of the dipoles are shown in Fig. 5. We verified that we obtained the desired defects by making a Burgers circuit around them (black atoms, see Fig. S2 in the SM [80] for details).

The dipole energy is

$$E_{\text{dipole}} = \frac{E_1 - E_0}{L_z}, \tag{2}$$

where E_0 is the energy of a system with a GB but no disconnection, E_1 is the energy of the same system with a disconnection dipole, and L_z is the width of the system along the disconnection lines. The dipole energy consists of core and step energies for each disconnection and an

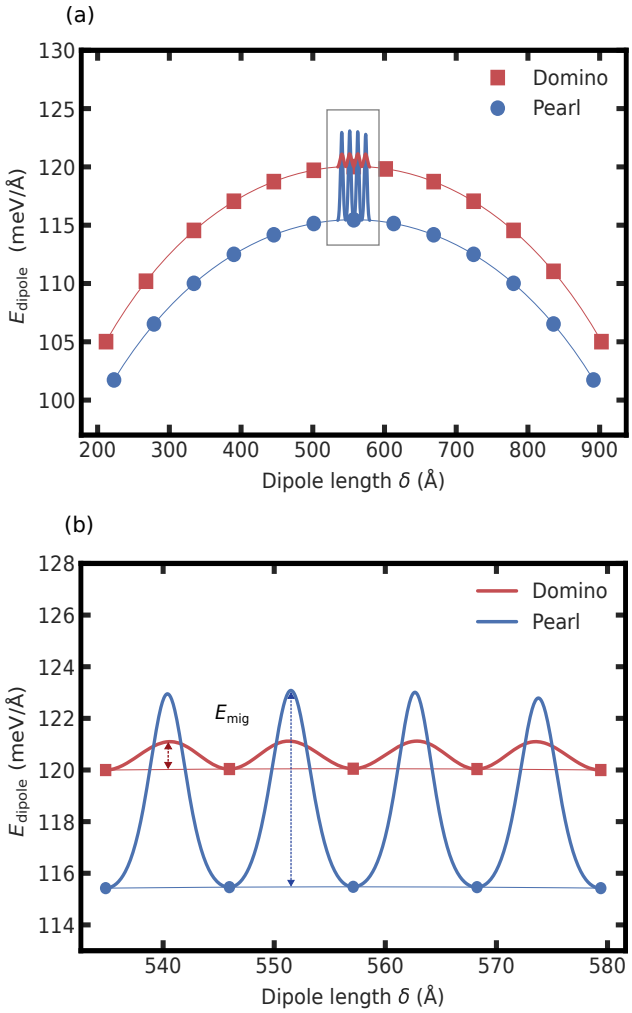

FIG. 6. (a) The formation energies E_{dipole} of disconnections for different dipole widths δ of the disconnection mode $(\mathbf{b}, h) = (0.586\,\text{Å}, 0.677\,\text{Å})$ are plotted for domino and pearl complexions. (b) Zoom of the gray area in (a). The energies of dipoles during their migration (thick lines) were obtained by NEB between the indicated local minima (squares and circles). The disconnection migration barrier E_{mig} is highlighted by red and blue arrows for domino and pearl.

elastic interaction energy [37, 47, 81, 82]:

$$\begin{aligned} E_{\text{dipole}} &= 2E_{\text{core}} + 2E_{\text{step}} + E_{\text{elastic}} \\ &= 2E_{\text{monopole}} + E_{\text{elastic}}. \end{aligned} \tag{3}$$

The monopole energy is thus the energy of a single, isolated disconnection. The elastic interaction energy is [82]

$$E_{\text{elastic}} = Kb^2 \ln\left(\frac{\delta}{\delta_c}\right), \tag{4}$$

where K is the energy coefficient describing the anisotropic crystal elasticity [82] and δ_c is the disconnection core size. Eqs. 3 and 4 can be simplified by a mathematical trick: we can "hide" the monopole energies by defining $\delta_0 = \delta_c \exp(-2E_{\text{monopole}}/(Kb^2))$ and writing

$$E_{\text{dipole}} = Kb^2 \ln\left(\frac{\delta}{\delta_0}\right). \tag{5}$$

The length δ_0 is now an effective core size without direct physical meaning, but Eq. 5 can be fitted directly to the dipole energies obtained by molecular statics simulations without knowledge of E_{monopole}. With periodic boundary conditions along the x and z directions in a bicrystal simulation, the energy of pair of disconnections is given by [27, 37, 44]

$$E_{\text{dipole}} = Kb^2 \ln\left(\frac{\sin(\pi\delta/L_x)}{\sin(\pi\delta_0/L_x)}\right), \tag{6}$$

taking into account the image interactions. When L_x is infinite, Eq. 6 reduces to Eq. 5. In our simulations, we have to consider the periodic case with a simulation box size of $1114.220\,\text{Å} \times L_y \times 6.261\,\text{Å}$. We varied L_y to verify that there are no size effects. Table I lists the GB energies

$$\gamma = \frac{E_1 - E_{\text{fcc}}}{L_x L_z} \tag{7}$$

for the different box sizes. Here, E_1 is the energy of a system containing a GB with a disconnection dipole and E_{fcc} is the energy of the same system without a GB. For simplicity, we report γ^*, which is the value for a dipole width $\delta^* = L_x/2$. These values converge at $L_y = 1929.540\,\text{Å}$, which are the results we report here. We do not use the larger box sizes in the main text of this paper, since we also performed NEB calculations on this system, which have convergence issues at larger system sizes. More data is provided in Figs. S3–S4 in the SM [80]. The resulting dipole energies are plotted in Fig. 6(a) and we list the fit parameters K and δ_0 in Table I. These parameters are comparable to those in a previous study on a $\Sigma 13$ tilt GB in copper [27] (see Appendix C for details). The parameter $K_{\text{domino}} \approx 76.8\,\text{meV}/\text{Å}^3$ for domino and $K_{\text{pearl}} \approx 76.4\,\text{meV}/\text{Å}^3$ for pearl is the same because it is a result of long-range interactions which are solely due to the Burgers vector. Methods were developed to directly calculate K from the stiffness tensor of the crystal, while taking into account the crystal anisotropy [82–85]. Following the methods of Eshelby et al. [83] and Stroh [85], we also obtained $K = 76.7\,\text{meV}/\text{Å}^3$, matching the fitted value.

Furthermore, we also calculated E_{monopole} by performing simulations with a single disconnection and open boundaries in x direction (with a monopole, periodic boundaries are not possible). We found that the absolute monopole energy does not converge even at large L_x (see Table S1 in the SM [80]), likely due to elastic interactions of the disconnection with the surfaces. The monopole energy difference between domino and pearl, however, did converge. For $L_x = 3342.799\,\text{Å}$, we obtain a monopole

energy of 73.5 meV/Å for domino and 70.7 meV/Å for pearl, resulting in a difference of 2.8 meV/Å.

The energy of the disconnection dipole is maximum at a disconnection dipole width $\delta^* = L_x/2$ is

$$E^*_{\text{dipole}} \approx Kb^2 \log\left(\frac{L_x}{\pi\delta_0}\right) \tag{8}$$

for periodic boundary conditions and the approximation is valid when $\delta_0/L_x \ll 1$. We obtained K and δ_0 from atomistic simulations by fitting Eq. 6, and hence E^*_{dipole} can be calculated for any given L_x of the simulation cell. Together with the difference in monopole energies, we can now obtain the ratio of true core sizes by separating $\delta_0^{\text{domino}}/\delta_0^{\text{pearl}}$ back into $\delta_c^{\text{domino}}/\delta_c^{\text{pearl}}$ and $\Delta E_{\text{monopole}}$ (cf. Eqs. 3–5; results in Table I). The core size of the disconnection in domino is 4–5% larger than in pearl.

All results indicate that it is easier to form disconnection dipoles in pearl than in domino. Our earlier results, however, were that pearl needs a higher critical stress for GB migration. It is clear that the formation energies cannot explain our observations.

D. Disconnection migration barriers

Apart from their formation, disconnections also need to move in order to facilitate GB migration. In analogy to bulk dislocations, there is also a Peierls barrier E_{mig} for disconnections, requiring a critical Peierls–Nabarro stress τ_{mig} to move [44, 45, 47, 81, 86, 87]. The atomic configuration at the saddle point of this barrier is not stable and can therefore not be explored with simple molecular statics calculations. The minimum energy path for the migration of a disconnection along the GB, extending the dipole width from δ_1 to δ_2, was calculated using NEB. We built two simulation boxes with dipoles that differ in spacing by a single GB unit cell (11.142 Å), which is the smallest distance between metastable configurations. This can be repeated for different δ_1 and δ_2 to obtain a continuous path as a function of δ. Figure 6 shows the results of four NEB calculations superimposed on the results from static calculations. It is clear that E_{mig} is much higher for pearl (7.6 meV/Å as compared to 1.1 meV/Å for domino), leading to a steeper energy landscape during disconnection migration. These values of E_{mig} are of similar magnitude as for a different, Σ13 tilt GB in copper, which had a barrier of 5.2 ± 0.4 meV/Å [27]. In our case, the differences between domino and pearl might be explained by the disconnection core size differences in domino and pearl (Table I). Similar to dislocations [81, 87, 88], the larger disconnection core size (spread out core) in domino compared to pearl might correlate with the lower Peierls barrier E_{mig}. This steepness of the energy landscape in pearl results in its higher GB migration stresses, despite the lower disconnection formation energies.

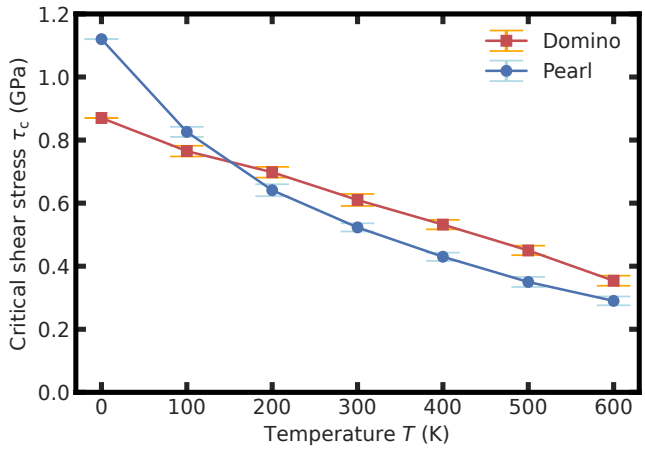

FIG. 7. The critical shear stress τ_c as a function of temperature. At temperatures of around 200 K and above, the critical stress τ_c of pearl drops below the one for domino.

E. Temperature effects and critical stresses

We proceeded to simulate the critical stress τ_c at finite temperatures up to $T = 700$ K. With the applied shear we found that the metastable domino phase transitions to pearl immediately at 700 K and above, so that meaningful stress values cannot be extracted. (The domino complexion is metastable over the whole temperature range [55], but the higher temperatures accelerate its transition to pearl even within the short simulation timescale.) We restrict ourselves therefore to the temperature range up to 600 K. We averaged the critical stress over several migration events (which are each equal to a stress drop), each time recording the maximum of the stress curve. The results are shown in Fig. 7 and are of similar magnitude as other GBs in fcc metals (see Appendix C). Interestingly, the critical stress for pearl is only higher than for domino up to a point between 100 K and 200 K. If we compare the Peierls barrier E_{mig} to the absolute formation energy E_{dipole}, however, we notice that the former is quite small (Fig. 6). Only due to its steepness, is it connected to a high stress. It is conceivable that the thermal energy would be sufficient to help overcome this small barrier, so that in the end only the formation energy matters. We tested this by starting with systems that already have a disconnection dipole of width $\delta^* = L_x/2$ inserted before applying shear. We can thus probe only τ_{mig}, the critical stress for disconnection migration. Figure 8(a) shows that domino has $\tau_{\text{mig}} \approx 0$ GPa, while pearl has $\tau_{\text{mig}} \approx 0.5$ GPa. The difference in τ_c (Fig. 4) is roughly 0.27 GPa, which is smaller. That is not surprising, since there is also a higher stress connected to the nucleation of domino. With increasing T, however, the disconnection migration barrier can be overcome more and more easily, resulting in $\tau_{\text{mig}} \approx 0$ GPa for both domino and pearl already at $T = 200$ K [Fig. 8(b)–(d)]. This can explain the temperature dependence: It is easier to nucleate dis-

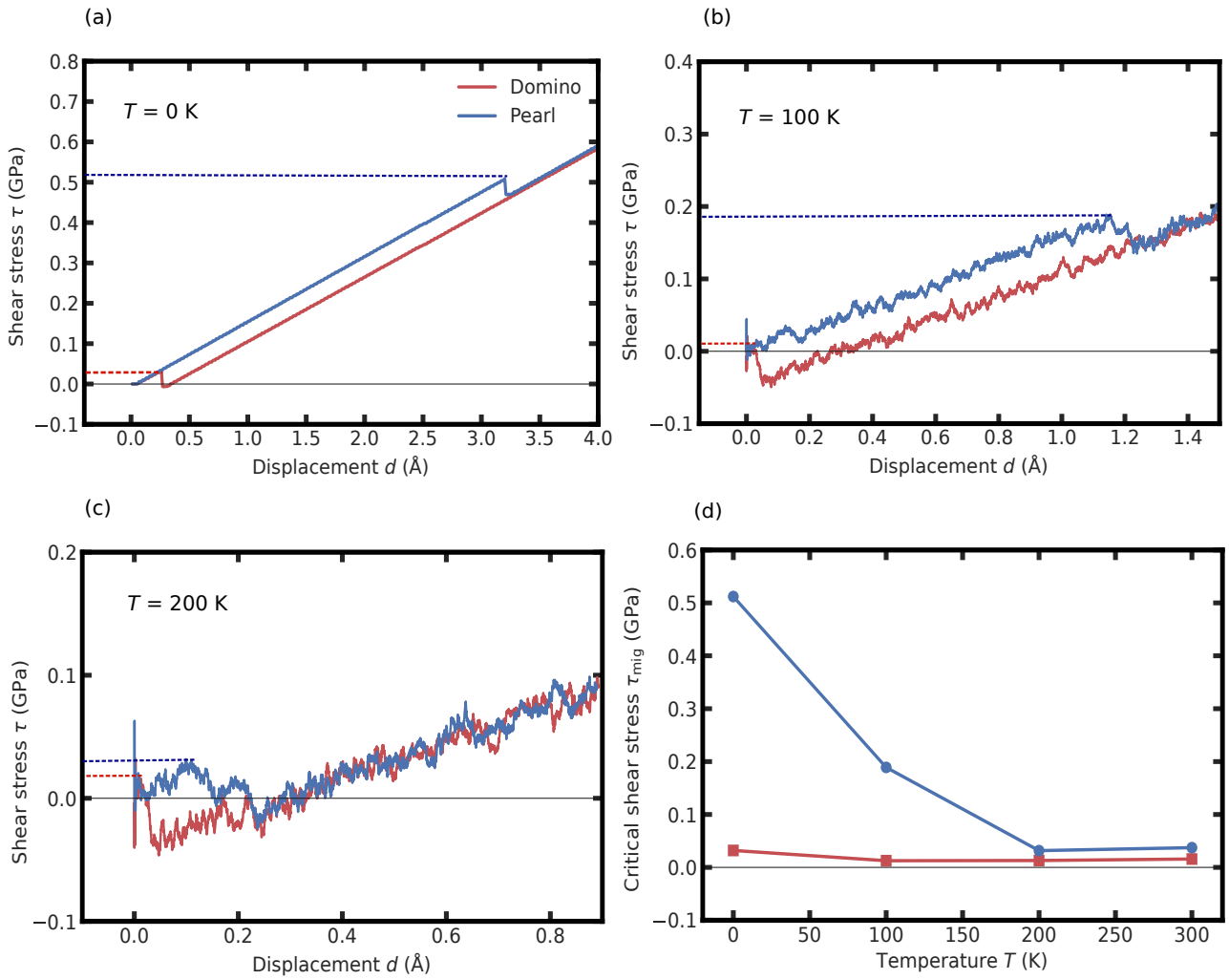

FIG. 8. (a)–(c) Shear stress–displacement curves for GBs with pre-existing disconnection dipoles of width $\delta^* = L_x/2$. The shear stress response to displacement at temperatures (a) 0 K, (b) 100 K, and (c) 200 K is plotted. The critical stress τ_{mig} for disconnection migration is indicated by the horizontal dotted lines. (d) It reduces with increasing temperature, dropping to close to zero at 200 K and above for both domino and pearl.

connections in the pearl complexion, but at low temperatures these disconnections have to cross high barriers to move. These barriers, however, are only high compared to domino and can be overcome with thermal energy. At room temperature and above, pearl GBs are easier to migrate since the GB migration is limited by defect nucleation.

IV. CONCLUSION

We used MD simulations to investigate the nucleation and migration of disconnections as the elementary mechanisms of shear coupled motion in Σ19b symmetric tilt GBs in Cu. In our clean GBs under periodic boundary conditions, the migration is a cycle of a disconnection dipole nucleating, growing, and annihilating. These GBs exhibit two complexions, domino and pearl, which migrate via the same disconnection mode ($\mathbf{b} = [0.586, 0, 0]$ Å, $h = 0.677$ Å). This mode corresponds to the shortest possible DSC vector, which also lies in the GB plane, leading to conservative motion of the GB. However, the critical shear stress τ_c required to move the GBs differs between the two complexions. At low temperatures, we found by comparing the disconnection dipole formation and migration energies of both the complexions, that the difference in shear stress is predominantly due to the steeper Peierls-like barrier in pearl. This is caused by the differences in atomic structure, in particular the core structure of the disconnections. We observed that pearl becomes easier to move than domino at around 200 K and above. By investigating the stress required to move a pre-existing disconnection dipole, we found that this stress becomes close to zero at these temperatures,

indicating that the GB migration barrier is then dominated by the dipole nucleation. We found that disconnections in domino have higher formation energies, but very low disconnection migration barriers. This explains why the critical shear stress for pearl changes steeply from being much higher than for domino to lower than domino between 0 K and 300 K. Future work will have to consider imperfect GBs and the interaction with dislocations and nonconservative disconnections to get a full picture of GB migration.

ACKNOWLEDGMENTS

The authors thank Nicolas Combe and Anupam Neogi for helpful discussions. This project has received funding from the European Research Council (ERC) under the European Union's Horizon 2020 research and innovation programme (Grant agreement No. 787446; GB-CORRELATE).

Appendix A: Disconnection modes from bicrystallography

The possible disconnections modes for a given GB—consisting of a set of Burgers vectors and step heights ($\mathbf{b}$,h)—can be obtained from its bicrystallography. For a certain $\mathbf{b}$, there are multiple possible step heights h. Figure 9 shows the dichromatic pattern of our Σ19b $[11\bar{1}]$ (178) GB. To describe $\mathbf{b}$, the notation $\mathbf{b}_{j/k}$ is used [89], where j and k are integers indicating the ending (j) and starting (k) plane of the vector. The planes are counted from a coincidence site, as demonstrated for $\mathbf{b}_{1/-1}$ in Fig. 9, where the dashed lines indicate the starting plane (-1) and the ending plane (1). The integers j and k can be multiplied with the unit step height $h_0 = a/(2|178|)$ to obtain the absolute length of the component normal to the GB. Four examples of Burgers vectors of low magnitude, i.e., $\mathbf{b}_{-15/-15}$, $\mathbf{b}_{-6/-9}$, $\mathbf{b}_{-7/-8}$, and $\mathbf{b}_{1/-1}$, are marked in Fig. 9. There are six Burgers vectors in total with the same length as $\mathbf{b}_{-15/-15}$ and $\mathbf{b}_{-6/-9}$, which have a magnitude of 0.586 Å. There are another six Burgers vectors of the same length as $\mathbf{b}_{-7/-8}$ and $\mathbf{b}_{1/-1}$, which shift the top grain position from a given $[11\bar{1}]$ plane to an adjacent $[11\bar{1}]$ plane, which have a magnitude of 2.114 Å. The in-plane shifts move identical symbol types, while $\mathbf{b}_{j/k}$ with out-of-plane component move any symbol on one of a different type. The Burgers vector $\mathbf{b}_{-15/-15}$ is the shortest vector that lies in the GB plane (pointing in ⟨532⟩ direction). This is favorable for the mobility of the corresponding disconnection, because its glide plane lies in the GB plane. The disconnections $\mathbf{b}_{-6/-9}$, $\mathbf{b}_{-7/-8}$, and $\mathbf{b}_{1/-1}$ have components normal to the GB plane and the disconnection motion would require climb in addition to glide. This can be understood by considering that the glide plane of the disconnection would no longer be equal to the GB plane, but that the disconnection can

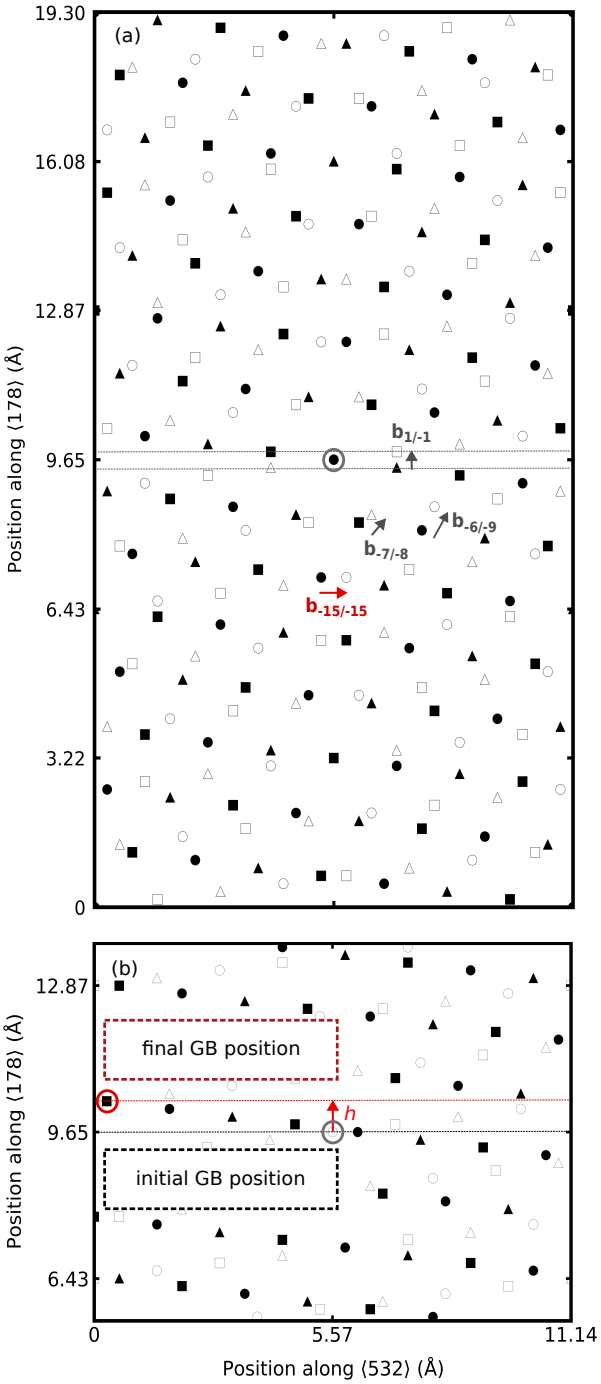

FIG. 9. (a) Dichromatic pattern of the Σ19b $[11\bar{1}]$ (178) symmetric tilt GB in the xy plane. White and black symbols represent the atoms from the two different grains. Circle, triangle, and square indicate different layers along z. Four unique DSC vectors of low magnitude are marked by arrows. The DSC vector $\mathbf{b}_{-15/-15}$ is marked with a red arrow and lies within the (178) GB plane, while $\mathbf{b}_{-6/-9}$, $\mathbf{b}_{-7/-8}$, and $\mathbf{b}_{1/-1}$ have components normal to the GB plane. (b) Pattern after moving the top crystal by $\mathbf{b}_{-15/-15}$. If we imagine that the original GB plane passed through the coincidence site marked by a gray circle, the new GB plane must also pass through a coincidence site (red circle) and has thereby moved by h. The same is true for an initial GB plane at any other position.

only exist on the GB plane. The resulting requirement of climb involves diffusion of vacancies in and out of the disconnection and is therefore slow. The disconnections $\mathbf{b}_{-7/-8}$ and $\mathbf{b}_{1/-1}$ are longer than $\mathbf{b}_{-15/-15}$ and $\mathbf{b}_{-6/-9}$ and likely have a higher core energy. It is thus likely that the shear-coupled motion is driven by $\mathbf{b}_{-15/-15}$ disconnections.

We can get the step height caused by a Burgers vector from the the dichromatic pattern. When the top crystal moves by $\mathbf{b}_{-15/-15}$, the original coincidence site (gray circle) shifts to a new position (red circle) along $\langle 178 \rangle$. The difference in old and new position of coincidence site along $\langle 178 \rangle$ is the step height (GB migration distance) h of 0.677 Å, as shown in Fig. 9(b). This disconnection is thus represented as disconnection mode $(\mathbf{b}, h) = ([0.586, 0, 0]\,\text{Å}, 0.677\,\text{Å})$. The ratio of shear displacement (equal to b_x) to GB migration distance (equal to h) is thus $\beta = b_x/h = 0.865$. This corresponds to the value obtained from the simulations in Sec. III A. Together with $\mathbf{b}_{-15/-15}$ being the shortest Burgers vector lying in the GB plane, this provides strong evidence that this is the active disconnection mode during shear-coupled GB migration in domino and pearl.

Appendix B: Atomic shuffling during GB migration

The perfect GBs in our simulations thus went through a cycle of nucleating, propagating and annihilating the $\mathbf{b}_{-15/-15}$ disconnection. Since we seem to observe the same disconnection mode for domino and pearl (same β), the differences in shear stress required to move the disconnection can also be due to the differences in the atomic shuffling during GB migration for both the complexions [49, 91].

The atomic shuffling during GB migration for both the complexions was observed after 20 shear stress drops in the molecular statics calculations (corresponding to $n = 20$ unit steps of GB migration). The mean GB plane moved a total distance of $nh = 13.540$ Å along y and the shear displacement $20d_s = n|\mathbf{b}| = 11.720$ Å along x for both the complexions. In Fig. 10, the initial positions of the atoms in the top and bottom grain before GB migration are plotted in black and their final positions after migration are marked in red and blue for domino and pearl, respectively. At first glance, we can see that the dichromatic pattern appears in the traversed region. This is as expected, due to the rearrangement of atoms in this regions from the crystallography of the top crystal (black, before) to the one of the bottom crystal (red/blue, after) [92, 93]. On closer inspection, it can be seen that there are no true coincidence sites, which is a result of the microscopic degrees of freedom of the GB: The dichromatic pattern is always plotted such that coincidence sites exist, but in reality the top crystal can always be translated arbitrarily against the bottom crystal [57, 63, 94]. Furthermore, a more complex pattern arises above/below the traversed region. It appears that atoms do not directly

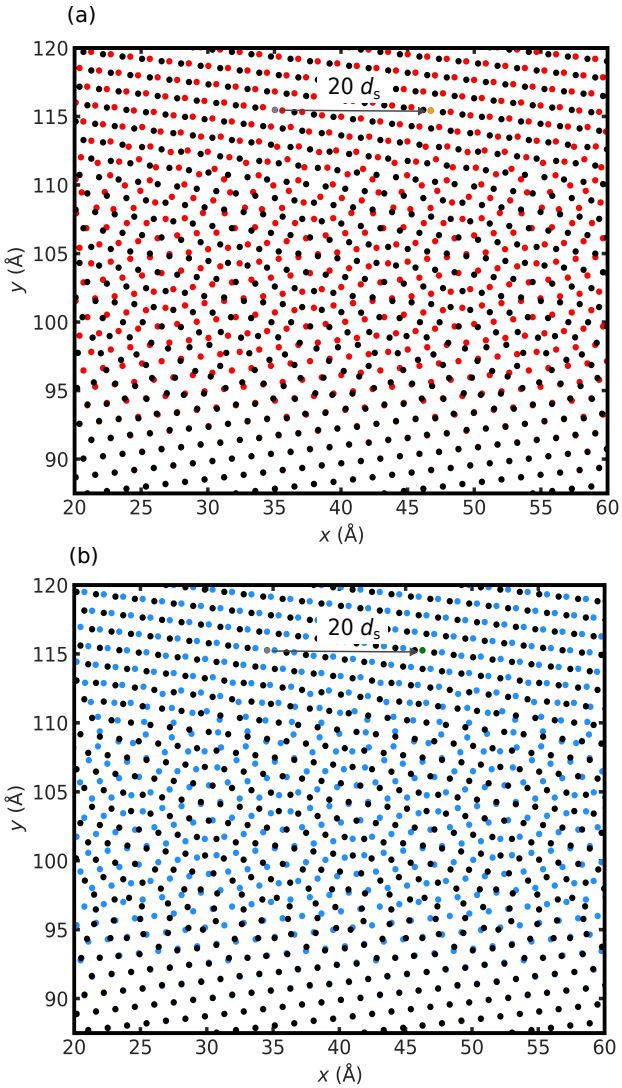

FIG. 10. Atom positions in (a) domino and (b) pearl before (black) and after (red/blue) shear-coupled GB motion. These images are after $n = 20$ unit steps of GB migration, which correspond to a GB migration distance of $nh = 13.540$ Å along y and a shear displacement $n|\mathbf{b}| = 20d_s = 11.720$ Å along x. In the traversed region, an image similar to the dichromatic pattern appears due to overlaying atoms from before the migration, which belong to the top crystal, and after the migration, which now belong to the bottom crystal. An additional offset between the atoms in the pattern is due to the microscopic degrees of freedom, i.e., the top and bottom crystal are shifted against each other depending on the complexion. Furthermore, the pattern at the start and end of the migration region is somewhat smeared out, indicating that the atomic jumps during the GB migration do not necessarily go from the initial to the final position, but can also occupy intermediary positions.

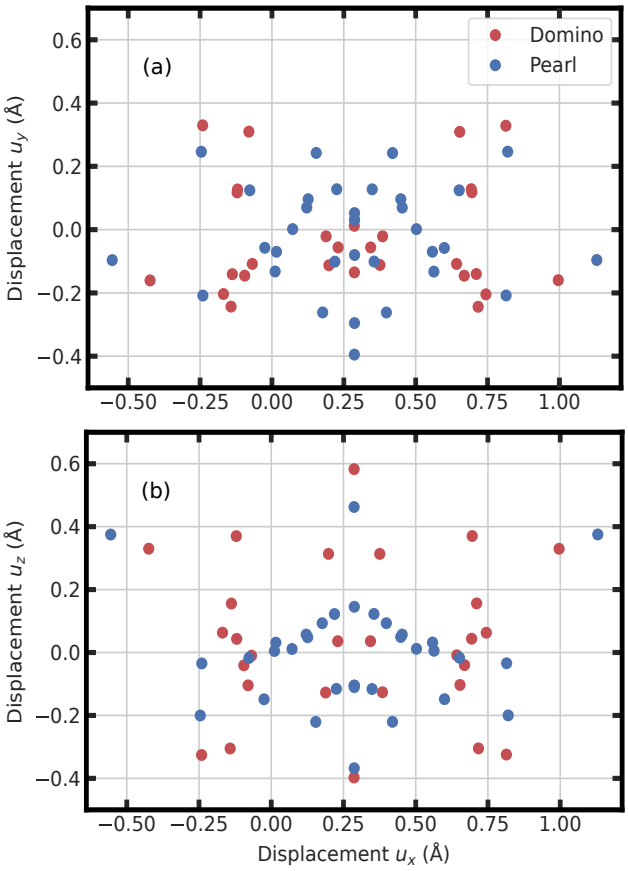

FIG. 11. Displacements of the atoms in the GB during a single GB migration step, plotted by (a) u_x and u_y components and (b) u_x and u_z components. Here, we define GB atoms as those atoms that were not identified as fcc either before or after the migration event by the polyhedral template matching method [90] in OVITO [73]. The displacements are symmetric around $|\mathbf{b}|/2 = 0.293$ Å in x direction.

jump from their initial to their final position during one GB migration step.

Hence we analyzed the atomic displacements during a single step of GB migration. A simulation cell of size $11.142 \times 192.291 \times 6.261$ Å^3 ($1 \times 10 \times 1$ units cells, 1137 atoms) was used for this. We only considered atoms that were not identified as fcc atoms either before or after the GB migration step, utilizing the polyhedral template matching structure identification method [90] as implemented in OVITO [73]. The results are shown in Fig. 11. The jump vectors are symmetric around $|\mathbf{b}|/2 = 0.586$ Å$/2 = 0.293$ Å in x direction. The average of all jumps has to be $|\mathbf{b}|/2$ because the displacement for atoms with y coordinates below the GB has to be zero, while the displacement above the GB has to be $|\mathbf{b}|$. The additional symmetry of the jump vectors is due to the symmetry of the GB. The atomic displacements during a single GB migration step do not correspond to DSC vectors. In our simulations, atoms thus transition from one crystallite to the GB region and only then to the second crystallite during GB migration. The non-DSC nature of the jump vectors is due to the internal degrees of freedom for the atomic positions of the domino and pearl complexions.

We furthermore probed the effort required to effect those jumps by calculating the L^2-norm of a combined vector of the displacement components for the GB atoms i as $\sqrt{\sum_{i=1}^{n}(x_i^2 + y_i^2 + z_i^2)}$. The atomic jump lengths is evaluated to be 3.018 Å for domino and 2.877 Å for pearl. The difference in jump lengths is small and seems to be unlikely to explain the differences in τ_c for the two complexions. It is therefore necessary to calculate the exact energy cost of introducing the disconnections as in Sec. III C.

Appendix C: Shear coupled motion in other GBs of fcc metals

The energy of disconnections depends on both their core and step energy and their elastic interaction energy, and is therefore best described by the parameters K and δ_0 (see Sec. III C). Here, K encodes the elasticity of the crystal lattice and δ_0 the properties of the disconnection core. Only a limited number of studies list such values, and for copper GBs we just found Ref. [27], in which as $\Sigma 13$ [001] (320) symmetric tilt GB is simulated. They obtained a value of $K = 30.468$ meV/Å^3, whereas we found $K = 76.7$ meV/Å^3 (Sec. III C). The difference could be a result of the anisotropy of copper and the different GB planes. The paper reported $E_{\text{monopole}} = 5.3$ meV/Å and $\delta_c = 3.615$ Å. The latter was chosen arbitrarily and we therefore combined these values into $\delta_0 = 2.556$ Å (see Eq. 5 and surrounding discussion), which is of the same order of magnitude as our values of $\delta_0 = 3.8$–4.4 Å (Table I). The migration barrier E_{mig} was reported as 5.2 ± 0.4 meV/Å, which is in the same range as our values of $E_{\text{mig}} = 1.1$–7.6 meV/Å (Sec. III D).

Previously, the critical shear stress τ_c was calculated for various GBs in fcc metals. Values lie in the range of 1–4 GPa. At 0 K, shear stress in $\Sigma 13$ [001] (320) and $\Sigma 17$ [001] (410) symmetric tilt Cu GBs is observed to be 1.4 GPa and 2.1 GPa, respectively [27, 46]. Likewise, shear stress in the $\Sigma 41$ [001] (540) Al GB is noted to be 2.85 GPa [95]. This is in the same range as our 0 K values, which are 1.117 GPa for pearl and 0.849 GPa for domino. Shear stress as a function of temperature is reported for complexions in Cu $\Sigma 5$ [001] (210) GB [69]. At 500 K, shear stress is observed to be ≈ 0.95 GPa and ≈ 0.58 GPa for split kite and filled kite complexions, respectively. At the same temperature, the critical shear stress in our domino and pearl complexions is ≈ 0.5 GPa and ≈ 0.4 GPa, respectively. The shear stress difference between the complexions can be due to the activation of different disconnection modes in, e.g., split kites and filled kites contrary to domino and pearl.

[1] V. Randle, Grain boundary engineering: an overview after 25 years, Materials Science and Technology **26**, 253 (2010).

[2] C. J. Simpson, K. T. Aust, and W. C. Winegard, The four stages of grain growth, Metallurgical Transactions **2**, 987 (1971).

[3] G. Riontino, C. Antonione, L. Battezzati, F. Marino, and M. C. Tabasso, Kinetics of abnormal grain growth in pure iron, Journal of Materials Science **14**, 86 (1979).

[4] H. V. Swygenhoven, A. Caro, and D. Farkas, Grain boundary structure and its influence on plastic deformation of polycrystalline FCC metals at the nanoscale: a molecular dynamics study, Scripta Materialia **44**, 1513 (2001).

[5] Z. Shan, E. A. Stach, J. M. K. Wiezorek, J. A. Knapp, D. M. Follstaedt, and S. X. Mao, Grain boundary-mediated plasticity in nanocrystalline nickel, Science **305**, 654 (2004).

[6] M. Meyers, A. Mishra, and D. Benson, Mechanical properties of nanocrystalline materials, Progress in Materials Science **51**, 427 (2006).

[7] J. Lohmiller, M. Grewer, C. Braun, A. Kobler, C. Kübel, K. Schüler, V. Honkimäki, H. Hahn, O. Kraft, R. Birringer, and P. A. Gruber, Untangling dislocation and grain boundary mediated plasticity in nanocrystalline nickel, Acta Materialia **65**, 295 (2014).

[8] H. V. Swygenhoven and P. M. Derlet, Grain-boundary sliding in nanocrystalline fcc metals, Physical Review B **64**, 10.1103/physrevb.64.224105 (2001).

[9] T. G. Langdon, Grain boundary sliding revisited: Developments in sliding over four decades, Journal of Materials Science **41**, 597 (2006).

[10] L. Wang, Y. Zhang, Z. Zeng, H. Zhou, J. He, P. Liu, M. Chen, J. Han, D. J. Srolovitz, J. Teng, Y. Guo, G. Yang, D. Kong, E. Ma, Y. Hu, B. Yin, X. Huang, Z. Zhang, T. Zhu, and X. Han, Tracking the sliding of grain boundaries at the atomic scale, Science **375**, 1261 (2022).

[11] M. Murayama, J. M. Howe, H. Hidaka, and S. Takaki, Atomic-level observation of disclination dipoles in mechanically milled, nanocrystalline fe, Science **295**, 2433 (2002).

[12] J. W. Cahn and J. E. Taylor, A unified approach to motion of grain boundaries, relative tangential translation along grain boundaries, and grain rotation, Acta Materialia **52**, 4887 (2004).

[13] M. Upmanyu, D. Srolovitz, A. Lobkovsky, J. Warren, and W. Carter, Simultaneous grain boundary migration and grain rotation, Acta Materialia **54**, 1707 (2006).

[14] L. Wang, J. Teng, P. Liu, A. Hirata, E. Ma, Z. Zhang, M. Chen, and X. Han, Grain rotation mediated by grain boundary dislocations in nanocrystalline platinum, Nature Communications **5**, 10.1038/ncomms5402 (2014).

[15] S. L. Thomas, K. Chen, J. Han, P. K. Purohit, and D. J. Srolovitz, Reconciling grain growth and shear-coupled grain boundary migration, Nature Communications **8**, 10.1038/s41467-017-01889-3 (2017).

[16] M. Winning, G. Gottstein, and L. Shvindlerman, Stress induced grain boundary motion, Acta Materialia **49**, 211 (2001).

[17] M. Winning, G. Gottstein, and L. Shvindlerman, On the mechanisms of grain boundary migration, Acta Materialia **50**, 353 (2002).

[18] A. Suzuki and Y. M. Mishin, Atomic mechanisms of grain boundary motion, Materials Science Forum **502**, 157 (2005).

[19] J. W. Cahn, Y. Mishin, and A. Suzuki, Coupling grain boundary motion to shear deformation, Acta Materialia **54**, 4953 (2006).

[20] D. Gianola, S. V. Petegem, M. Legros, S. Brandstetter, H. V. Swygenhoven, and K. Hemker, Stress-assisted discontinuous grain growth and its effect on the deformation behavior of nanocrystalline aluminum thin films, Acta Materialia **54**, 2253 (2006).

[21] Y. Mishin, A. Suzuki, B. P. Uberuaga, and A. F. Voter, Stick-slip behavior of grain boundaries studied by accelerated molecular dynamics, Physical Review B **75**, 10.1103/physrevb.75.224101 (2007).

[22] V. A. Ivanov and Y. Mishin, Dynamics of grain boundary motion coupled to shear deformation: An analytical model and its verification by molecular dynamics, Physical Review B **78**, 10.1103/physrevb.78.064106 (2008).

[23] T. Gorkaya, D. A. Molodov, and G. Gottstein, Stress-driven migration of symmetrical ⟨100⟩ tilt grain boundaries in al bicrystals, Acta Materialia **57**, 5396 (2009).

[24] D. Caillard, F. Mompiou, and M. Legros, Grain-boundary shear-migration coupling. II. Geometrical model for general boundaries, Acta Materialia **57**, 2390 (2009).

[25] F. Mompiou, D. Caillard, and M. Legros, Grain boundary shear–migration coupling—I. In situ TEM straining experiments in Al polycrystals, Acta Materialia **57**, 2198 (2009).

[26] F. Mompiou, M. Legros, and D. Caillard, Direct observation and quantification of grain boundary shear-migration coupling in polycrystalline Al, Journal of Materials Science **46**, 4308 (2011).

[27] A. Rajabzadeh, F. Mompiou, M. Legros, and N. Combe, Elementary mechanisms of shear-coupled grain boundary migration, Physical Review Letters **110**, 10.1103/physrevlett.110.265507 (2013).

[28] J. Li and A. Soh, Toughening of nanocrystalline materials through shear-coupled migration of grain boundaries, Scripta Materialia **69**, 283 (2013).

[29] E. R. Homer, S. M. Foiles, E. A. Holm, and D. L. Olmsted, Phenomenology of shear-coupled grain boundary motion in symmetric tilt and general grain boundaries, Acta Materialia **61**, 1048 (2013).

[30] A. Rajabzadeh, F. Mompiou, S. Lartigue-Korinek, N. Combe, M. Legros, and D. Molodov, The role of disconnections in deformation-coupled grain boundary migration, Acta Materialia **77**, 223 (2014).

[31] Q. Zhu, G. Cao, J. Wang, C. Deng, J. Li, Z. Zhang, and S. X. Mao, In situ atomistic observation of disconnection-mediated grain boundary migration, Nature Communications **10**, 10.1038/s41467-018-08031-x (2019).

[32] J. Wei, B. Feng, R. Ishikawa, T. Yokoi, K. Matsunaga, N. Shibata, and Y. Ikuhara, Direct imaging of atomistic grain boundary migration, Nature Materials **20**, 951 (2021).

[33] M. Dao, L. Lu, R. Asaro, J. De Hosson, and E. Ma, Toward a quantitative understanding of mechanical behav-

ior of nanocrystalline metals, Acta Materialia **55**, 4041 (2007).
[34] V. Yamakov, D. Wolf, S. R. Phillpot, A. K. Mukherjee, and H. Gleiter, Dislocation processes in the deformation of nanocrystalline aluminium by molecular-dynamics simulation, Nature Materials **1**, 45 (2002).
[35] J. Hirth and R. Pond, Steps, dislocations and disconnections as interface defects relating to structure and phase transformations, Acta Materialia **44**, 4749 (1996).
[36] M. Ashby, Boundary defects, and atomistic aspects of boundary sliding and diffusional creep, Surface Science **31**, 498 (1972).
[37] J. Han, S. L. Thomas, and D. J. Srolovitz, Grain-boundary kinetics: A unified approach, Progress in Materials Science **98**, 386 (2018).
[38] K. Chen, J. Han, S. L. Thomas, and D. J. Srolovitz, Grain boundary shear coupling is not a grain boundary property, Acta Materialia **167**, 241 (2019).
[39] W. Bollmann, General geometrical theory of crystalline interfaces, in *Crystal Defects and Crystalline Interfaces* (Springer Berlin Heidelberg, 1970) pp. 143–185.
[40] J. Hirth and R. Balluffi, On grain boundary dislocations and ledges, Acta Metallurgica **21**, 929 (1973).
[41] J. Hirth, R. Pond, and J. Lothe, Disconnections in tilt walls, Acta Materialia **54**, 4237 (2006).
[42] A. Rajabzadeh, M. Legros, N. Combe, F. Mompiou, and D. Molodov, Evidence of grain boundary dislocation step motion associated to shear-coupled grain boundary migration, Philosophical Magazine **93**, 1299 (2013).
[43] N. Combe, F. Mompiou, and M. Legros, Disconnections kinks and competing modes in shear-coupled grain boundary migration, Physical Review B **93**, 10.1103/physrevb.93.024109 (2016).
[44] O. MacKain, M. Cottura, D. Rodney, and E. Clouet, Atomic-scale modeling of twinning disconnections in zirconium, Physical Review B **95**, 10.1103/physrevb.95.134102 (2017).
[45] K. Chen, J. Han, and D. J. Srolovitz, On the temperature dependence of grain boundary mobility, Acta Materialia **194**, 412 (2020).
[46] N. Combe, F. Mompiou, and M. Legros, Multiple coupling modes to relax shear strain during grain boundary migration, Acta Materialia **218**, 117222 (2021).
[47] H. Khater, A. Serra, R. Pond, and J. Hirth, The disconnection mechanism of coupled migration and shear at grain boundaries, Acta Materialia **60**, 2007 (2012).
[48] K. Chen, D. J. Srolovitz, and J. Han, Grain-boundary topological phase transitions, Proceedings of the National Academy of Sciences **117**, 33077 (2020).
[49] I. Chesser, E. Holm, and B. Runnels, Optimal transportation of grain boundaries: A forward model for predicting migration mechanisms, Acta Materialia **210**, 116823 (2021).
[50] T. Frolov, D. L. Olmsted, M. Asta, and Y. Mishin, Structural phase transformations in metallic grain boundaries, Nature Communications **4**, 10.1038/ncomms2919 (2013).
[51] M. Aramfard and C. Deng, Mechanically enhanced grain boundary structural phase transformation in Cu, Acta Mater. **146**, 304 (2018).
[52] Q. Zhu, A. Samanta, B. Li, R. E. Rudd, and T. Frolov, Predicting phase behavior of grain boundaries with evolutionary search and machine learning, Nature Communications **9**, 10.1038/s41467-018-02937-2 (2018).
[53] T. Frolov, Q. Zhu, T. Oppelstrup, J. Marian, and R. E. Rudd, Structures and transitions in bcc tungsten grain boundaries and their role in the absorption of point defects, Acta Mater. **159**, 123 (2018).
[54] C. Yang, M. Zhang, and L. Qi, Grain boundary structure search by using an evolutionary algorithm with effective mutation methods, Comput. Mater. Sci. **184**, 109812 (2020).
[55] T. Meiners, T. Frolov, R. E. Rudd, G. Dehm, and C. H. Liebscher, Observations of grain-boundary phase transformations in an elemental metal, Nature **579**, 375 (2020).
[56] L. Langenohl, T. Brink, R. Freitas, T. Frolov, G. Dehm, and C. H. Liebscher, Dual phase patterning during a congruent grain boundary phase transition in elemental copper, Nature Communications **13**, 3331 (2022).
[57] T. Brink, L. Langenohl, H. Bishara, and G. Dehm, Universality of grain boundary phases in fcc metals: Case study on high-angle [111] symmetric tilt grain boundaries, Physical Review B **107**, 054103 (2023).
[58] J. W. Gibbs, *The Collected Works of J. Willard Gibbs, Volume 1: Thermodynamics* (Yale University Press, New Haven, CT, USA, 1948).
[59] E. W. Hart, Two-dimensional phase transformation in grain boundaries, Scr. Metall. **2**, 179 (1968).
[60] J. W. Cahn, Transitions and phase equilibria among grain boundary structures, Le Journal de Physique Colloques **43**, C6 (1982).
[61] C. Rottman, Theory of phase transitions at internal interfaces, J. Phys. Colloques **49**, C5 (1988).
[62] T. Frolov and Y. Mishin, Thermodynamics of coherent interfaces under mechanical stresses. I. Theory, Physical Review B **85**, 10.1103/physrevb.85.224106 (2012).
[63] T. Frolov and Y. Mishin, Thermodynamics of coherent interfaces under mechanical stresses. II. Application to atomistic simulation of grain boundaries, Physical Review B **85**, 10.1103/physrevb.85.224107 (2012).
[64] M. Tang, W. C. Carter, and R. M. Cannon, Diffuse interface model for structural transitions of grain boundaries, Physical Review B **73**, 10.1103/physrevb.73.024102 (2006).
[65] S. J. Dillon, M. Tang, W. C. Carter, and M. P. Harmer, Complexion: A new concept for kinetic engineering in materials science, Acta Materialia **55**, 6208 (2007).
[66] P. R. Cantwell, M. Tang, S. J. Dillon, J. Luo, G. S. Rohrer, and M. P. Harmer, Grain boundary complexions, Acta Materialia **62**, 1 (2014).
[67] P. R. Cantwell, T. Frolov, T. J. Rupert, A. R. Krause, C. J. Marvel, G. S. Rohrer, J. M. Rickman, and M. P. Harmer, Grain boundary complexion transitions, Annual Review of Materials Research **50**, 465 (2020).
[68] T. Frolov and Y. Mishin, Phases, phase equilibria, and phase rules in low-dimensional systems, The Journal of Chemical Physics **143**, 044706 (2015).
[69] T. Frolov, Effect of interfacial structural phase transitions on the coupled motion of grain boundaries: A molecular dynamics study, Applied Physics Letters **104**, 211905 (2014).
[70] S. Plimpton, Fast parallel algorithms for short-range molecular dynamics, Journal of Computational Physics **117**, 1 (1995).
[71] A. P. Thompson, H. M. Aktulga, R. Berger, D. S. Bolintineanu, W. M. Brown, P. S. Crozier, P. J. in 't Veld, A. Kohlmeyer, S. G. Moore, T. D. Nguyen, R. Shan, M. J. Stevens, J. Tranchida, C. Trott, and S. J. Plimpton,

LAMMPS - a flexible simulation tool for particle-based materials modeling at the atomic, meso, and continuum scales, Computer Physics Communications **271**, 108171 (2022).

[72] Y. Mishin, M. J. Mehl, D. A. Papaconstantopoulos, A. F. Voter, and J. D. Kress, Structural stability and lattice defects in copper:*ab initio*, tight-binding, and embedded-atom calculations, Physical Review B **63**, 10.1103/physrevb.63.224106 (2001).

[73] A. Stukowski, Visualization and analysis of atomistic simulation data with OVITO–the open visualization tool, Modelling and Simulation in Materials Science and Engineering **18**, 015012 (2009).

[74] I. Winter, T. Oppelstrup, T. Frolov, and R. Rudd, Characterization and visualization of grain boundary disconnections, Acta Materialia **237**, 118067 (2022).

[75] I. Winter, R. Rudd, T. Oppelstrup, and T. Frolov, Nucleation of grain boundary phases, Physical Review Letters **128**, 10.1103/physrevlett.128.035701 (2022).

[76] G. Henkelman and H. Jónsson, Improved tangent estimate in the nudged elastic band method for finding minimum energy paths and saddle points, The Journal of Chemical Physics **113**, 9978 (2000).

[77] G. Henkelman, B. P. Uberuaga, and H. Jónsson, A climbing image nudged elastic band method for finding saddle points and minimum energy paths, The Journal of Chemical Physics **113**, 9901 (2000).

[78] D. Sheppard, R. Terrell, and G. Henkelman, Optimization methods for finding minimum energy paths, The Journal of Chemical Physics **128**, 134106 (2008).

[79] S. Pemma, R. Janisch, G. Dehm, and T. Brink, Dataset for "Elementary mechanisms of shear-coupled grain boundary migration for different complexions of a copper tilt grain boundary", Zenodo (2023).

[80] See Supplemental Material at [link to be inserted by publisher] for additional data.

[81] F. Nabarro, Mathematical theory of stationary dislocations, Advances in Physics **1**, 269 (1952).

[82] J. P. Hirth, J. Lothe, and T. Mura, Theory of dislocations (2nd ed.), Journal of Applied Mechanics **50**, 476 (1983).

[83] J. Eshelby, W. Read, and W. Shockley, Anisotropic elasticity with applications to dislocation theory, Acta Metallurgica **1**, 251 (1953).

[84] A. Foreman, Dislocation energies in anisotropic crystals, Acta Metallurgica **3**, 322 (1955).

[85] A. N. Stroh, Dislocations and cracks in anisotropic elasticity, Philosophical Magazine **3**, 625 (1958).

[86] R. Peierls, The size of a dislocation, Proc. Phys. Soc. **52**, 34 (1940).

[87] F. R. N. Nabarro, Dislocations in a simple cubic lattice, Proc Phys Soc **59**, 256 (1947).

[88] T. H. Courtney, *Mechanical Behavior of Materials*, McGraw-Hill series in materials science and engineering (McGraw-Hill, 2000).

[89] A. Serra and D. J. Bacon, A new model for 1012 twin growth in hcp metals, Philosophical Magazine A **73**, 333 (1996).

[90] P. M. Larsen, S. Schmidt, and J. Schiøtz, Robust structural identification via polyhedral template matching, Modelling and Simulation in Materials Science and Engineering **24**, 055007 (2016).

[91] I. Chesser, B. Runnels, and E. Holm, A taxonomy of grain boundary migration mechanisms via displacement texture characterization, Acta Materialia **222**, 117425 (2022).

[92] H. Zhang and D. J. Srolovitz, Simulation and analysis of the migration mechanism of $\sigma 5$ tilt grain boundaries in an fcc metal, Acta Materialia **54**, 623 (2006).

[93] C. P. Race, R. Hadian, J. von Pezold, B. Grabowski, and J. Neugebauer, Mechanisms and kinetics of the migration of grain boundaries containing extended defects, Physical Review B **92**, 10.1103/physrevb.92.174115 (2015).

[94] T. Frolov, D. L. Medlin, and M. Asta, Dislocation content of grain boundary phase junctions and its relation to grain boundary excess properties, Physical Review B **103**, 10.1103/physrevb.103.184108 (2021).

[95] M. Larranaga, F. Mompiou, M. Legros, and N. Combe, Role of sessile disconnection dipoles in shear-coupled grain boundary migration, Physical Review Materials **4**, 10.1103/physrevmaterials.4.123606 (2020).